Published in final edited form as:
Am J Orthod Dentofacial Orthop. 2013 December ; 144(6): 802–817. doi:10.1016/j.ajodo.2013.07.013.

Phantom dosimetry and image quality of i-CAT FLX cone-beam computed tomography

John B. Ludlow, DDS, MS, FDS, RCSEd[1,†] and **Cameron Walker, DDS, MS, PhD**[2]

[1]Professor, Department of Diagnostic Sciences, University of North Carolina School of Dentistry, Chapel Hill, North Carolina, USA

[2]Adjunct Assistant Professor, Faculty of Orthodontics, University of Missouri – Kansas City, School of Dentistry, Kansas City, Missouri, USA

Abstract

Introduction—Increasing use of cone-beam computed tomography in orthodontics has been coupled with heightened concern with the long-term risks of x-ray exposure in orthodontic populations. An industry response to this has been to offer low-exposure alternative scanning options in newer cone-beam computed tomography models.

Methods—Effective doses resulting from various combinations of field size, and field location comparing child and adult anthropomorphic phantoms using the recently introduced i-CAT FLX cone-beam computed tomography unit were measured with Optical Stimulated Dosimetry using previously validated protocols. Scan protocols included High Resolution (360° rotation, 600 image frames, 120 kVp, 5 mA, 7.4 sec), Standard (360°, 300 frames, 120 kVp, 5 mA, 3.7 sec), QuickScan (180°, 160 frames, 120 kVp, 5 mA, 2 sec) and QuickScan+ (180°, 160 frames, 90 kVp, 3 mA, 2 sec). Contrast-to-noise ratio (CNR) was calculated as a quantitative measure of image quality for the various exposure options using the QUART DVT phantom.

Results—Child phantom doses were on average 36% greater than Adult phantom doses. QuickScan+ protocols resulted in significantly lower doses than Standard protocols for child ($p=0.0167$) and adult ($p=0.0055$) phantoms. 13×16 cm cephalometric fields of view ranged from 11–85 μSv in the adult phantom and 18–120 μSv in the child for QuickScan+ and Standard protocols respectively. CNR was reduced by approximately 2/3rds comparing QuickScan+ to Standard exposure parameters.

Conclusions—QuickScan+ effective doses are comparable to conventional panoramic examinations. Significant dose reductions are accompanied by significant reductions in image quality. However, this trade-off may be acceptable for certain diagnostic tasks such as interim assessment of treatment results.

[†]North Carolina Oral Health Institute, Koury Oral Health Sciences, Room 5411-K, 385 South Columbia Street, Chapel Hill, NC 27599-7455, Office: 919-537-3141, Fax: 919-966-0705, jbl@email.unc.edu.

Dr. Walker participated in background research, data evaluation, and manuscript preparation
Dr. Ludlow participated in protocol development, data gathering, statistical evaluation, and manuscript preparation

Introduction and literature review

The use of cone-beam computed tomography (CBCT) in orthodontics has increased dramatically over the last few years.(1) Because cancer is the principal long-term biological effect of exposure to x-rays, one of the greatest issues facing CBCT in orthodontics is justification of the increased dose of ionizing radiation administered to patients compared to standard 2D imaging techniques.

A routine medical CT head scan may have an effective dose of approximately 2 mSv(2). While the majority of CBCT examinations have been reported to impart a much lower dose, CBCT units from different manufacturers have been shown to vary in patient dose 10 fold for an equivalent field of view (FOV), with some units roughly equivalent in dose to optimized CT scans(3). Although the risk to an individual from a single CT or CBCT examination may not itself be large, millions of exams are performed each year, making radiation exposure from dental and medical imaging an important public health issue. It has been estimated that from 1.5% to 2% of all US cancers may be attributed to computed tomography (CT) studies alone(4). This is especially important when considering the adolescent and pediatric populations that routinely receive orthodontic treatment in whom cellular growth and organ development is associated with increased radiosensitivity of tissues. In conjunction with a longer life expectancy in which cancer can develop, children may be two times to five times more sensitive to radiation carcinogenesis as mature adults(2, 5).

“Image quality” in CBCT is observer dependent, subjective and is used to describe how well desired information can be extracted from an image. Because it is subjective by nature, the measurement and comparison of image quality across CBCT units in diagnostic situations remains a complex problem. Two of the elements of subjective image quality that correlate with objective quality measures include contrast and spatial resolution (6). Image contrast can be objectively measured via the Contrast to Noise Ratio (CNR) while spatial resolution can be measured by computing a Modulation Transfer Function (MTF). The quality of CBCT scans is also an important consideration for users in orthodontics because a selection of image quality for a CBCT scan becomes a decision on dose and vice versa. Image quality technical factor adjustments that select between “high” and “low” image quality in many CBCT units can cause as much as 7 fold differences in dose(3).

The ongoing challenge in the optimization of CBCT is to reduce dose without drastically decreasing imaging quality and diagnostic information. A potential means of reducing patient risk from CBCT examinations is to limit the area of exposure by utilizing variable fields of view that are sized for the location of the anatomy of interest. However, voxel size is linked to FOV in many CBCT units and smaller voxel sizes associated with smaller FOVs may actually increase dose due to increases in exposure that are needed to maintain adequate CNR. Another approach is to reduce exposure for diagnostic tasks that theoretically require lower contrast to noise ratios or lower signal modulation transfer functions. An example of this type of task might be checking angulation of roots. The combination of careful selection of exposure parameters and field of view may result in an optimal use of dose for specific diagnostic tasks in orthodontic practice.

The purpose of this study was to evaluate doses resulting from various combinations of field size, location, and exposure parameters using child and adult phantoms with the i-CAT FLX unit. A second aim was to measure contrast to noise ratio (CNR) and modulation transfer function (MTF) as quantitative measures of image quality for the various exposure options offered by the i-CAT FLX. A tertiary aim was to compare phantom sizes and types as well as Thermoluminescent dosimetry (TLD) and Optically stimulated luminescent dosimetry (OSL).

Materials and Methods

Optically stimulated luminescent dosimeters (Nanodot, Landauer, Inc., Glenwood, IL) are plastic disks infused with aluminum oxide doped with carbon (Al_2O_3:C). The trace amounts of Carbon in the Al_2O_3 crystal lattice create imperfections that act as traps (F centers) for electrons or holes. After exposure to ionizing radiation, free electrons and holes are generated and trapped at the F centers in proportion to the amount of energy in the exposure. Energy captured by the F centers is reemitted as light when electrons or holes recombine. This occurs when the crystal is optically stimulated with a controlled exposure of 540 nm light from a light emitting diode. The energy released from F centers can be distinguished from the stimulating light because it is emitted in the form of 420 nm photons. The intensity of the emitted luminescence depends on the dose absorbed by the OSLD and the intensity of the stimulating light. This intensity is proportional to the stored dose and is recorded by a photomultiplier tube that incorporates a filter that screens out photons from the stimulating light source. Each dosimeter is encased in a light-tight plastic holder measuring approximately 1 mm × 10 mm × 10 mm. This case prevents loss of energy through stimulation by ambient light. Dosimeters used in this study were read with a portable reader (MicroStar, Landauer, Inc., Glenwood, IL). The reader was calibrated before use. Following calibration, photon counts from dosimeters may be recorded with an accuracy of ~+/− 2%. Photon counts are converted to dose using an energy specific conversion factor. Doses reported by the reader were adjusted for energy response using a 3^{rd} order polynomial calibration curve derived from side-by-side comparison of recorded doses from an ion chamber and OSL dosimeters over a range of 80 – 120 kVp using an adjustable kVp source. For this study, the OSL sensitivity at 90 kVp was estimated at .94 (mean kV = 60). OSL sensitivity at 120 kVp was estimated at 0.78 (mean kV = 80).

A software and hardware upgraded model of the i-CAT Next Generation dental CBCT unit (Imaging Sciences, Hatfield PA) was investigated in this study. The unit was updated to meet specifications that are named “i-CAT FLX”. Volume scans for this unit range from 8 cm × 8 cm to 23 cm × 17 cm. The unit operates at 90 kVp or 120 kVp and 3 or 5 mA with a pulsed exposure time from 2.0 to 7.4 seconds. The unit rotates through 360° over 8.6 or 26 seconds. A 180° rotation is also available with a rotation time of 4.8 seconds. Scan parameters used for child and adult phantoms are seen in Table 1.

Adult dosimetry was acquired using a tissue equivalent phantom simulating the anatomy of an average adult male (Atom Max Model 711 HN, CIRS Inc., Norfolk, VA). The phantom includes detailed 3D anthropomorphic anatomy including brain, bone, larynx, trachea, sinus, nasal cavities and teeth. The bones contain both cortical and trabecular separation. The phantom was modified by machining slots to accept Nanodot dosimeters at sites corresponding to internal tissues of interest. A skin surface dosimeter in the back of the neck is positioned at the vertical center of the designated slice level and taped in position. Lens of eye dosimeters are centered over and inset in the anatomic location for the lens and taped in position. Internal dosimeters are positioned vertically with the upper edge of the dosimeter slot, flush with the surface of the selected slice level and held in position by friction of the dosimeter case and the phantom material at the sampled anatomic location. Adult dosimeter anatomic locations and phantom levels are seen in (Figure 1). During scanning, the phantom was oriented with its section planes approximately parallel to the scan rotation plane (horizon). A phantom position simulating positioning of a patient on the chin rest was used. With the exception of the 13 × 16 cm cephalometric and 6 × 16 cm maxillary FOVs, centered FOVs were positioned to capture approximately 5 mm of soft tissue below the lower cortical border of the chin. Anterior-posterior position of the phantom was established to capture approximately 5 mm of soft tissue anterior to the facial surface of the maxillary incisor crown. For 6 × 16 cm maxillary views, the lower border of the FOV was positioned approximately 5 mm below the maxillary central incisor edge. For 13 × 16 cephalometric views, the tip of the nose and the lower soft tissue border of the chin were included in the field of view (Figure 2).

Child dosimetry was acquired using a tissue equivalent phantom simulating the anatomy of a ten-year old child (Atom Model 706 HN, CIRS Inc., Norfolk, VA). Tissues simulated in the ATOM phantom are average soft tissue, average bone tissue, spinal cord, spinal disks, brain and sinus. Simulated bone tissue matches age-related density. Dosimeter anatomic locations and child phantom levels are seen in (Figure 3). With the exception of the 11 × 16 cm, 13 × 16 cm and 6 × 16 cm maxillary FOVs, centered FOVs were positioned to capture approximately 5 mm of soft tissue below the lower cortical border of the chin. Anterior-posterior position of the phantom was established to capture approximately 5 mm of soft tissue anterior to the facial surface of the maxillary incisor crown. For 6 × 16 cm maxillary views, the lower border of the FOV was positioned approximately 5 mm below the maxillary central incisor edge. For 11 × 16 and 13 × 16 cephalometric views, the tip of the nose and the lower soft tissue border of the chin were included in the field of view (Figure 4).

Two to twelve exposures were utilized for each dosimeter run to provide a more reliable measure of radiation in the dosimeters. Smaller FOVs require more exposure repetition because more dosimeters are outside of the field of direct exposure and absorb only small quantities of scatter radiation. For every scan, a scout view was also acquired. Doses recorded by the OSLD reader were divided by the number of scans to determine the ‘exposure per examination’ for each dosimeter.

Doses from OSLDs at different positions within a tissue or organ were averaged to express the average tissue-absorbed dose in micrograys (μGy). The products of these values and the percentage of a tissue or organ irradiated in a radiographic examination (Table 2) were used to calculate the equivalent dose (H_T) in micro-Sieverts (μSv) (7).

For bone, the equivalent dose to the whole-body bone surface was calculated using the summation of the individual equivalent doses to the calvarium, the mandible, and the cervical spine. The determination of these equivalent doses is based on the distribution of bone throughout the body: the mandible contains 1.3%, the calvaria, 11.8%, and the cervical spine, 3.4% (8). Distribution of adult bone marrow is calculated using an average of data from Christy for 25 and 40 year olds(9). The mandible contains 0.8%, the calvaria, 7.7%, and the cervical spine, 3.8% of the adult marrow distribution. The 10 year-old child marrow distribution is calculated as 1.1% for the mandible, 11.6% for the cranium, and 2.7% for the cervical spine for a total of 15.4% of the total body marrow.

Following the technique of Underhill and co-authors, three locations within the calvarium were averaged to determine calvarial dose(8). For bone, a correction factor based on experimentally determined mass energy attenuation coefficients for bone and muscle irradiated with mono-energetic photons was applied. An effective beam energy estimated to be 2/3rds of the peak beam energy of the x-ray unit was used to determine bone/muscle attenuation ratios. A linear fit (R^2=0.996) of ratios from 40 to 80 kV from published data (10) produced the following equation: bone/muscle attenuation ratio = −0.0618 × kV peak × 2/3 + 6.9406. Values calculated from this equation provided a bone/muscle attenuation ratio of 3.21 at 60 kV (90 kV peak) and 1.97 at 80 kV (120 kV peak).

NIH-PA Author Manuscript

NIH-PA Author Manuscript

The proportion of skin surface area in the head and neck region directly exposed during maxillofacial CBCT imaging is estimated as 5% of the total body to calculate radiation weighted dose to the skin following the procedure Ludlow and co-authors(11). Similarly, muscle and lymphatic nodes exposures are estimated to represent 5% of the total body complement for these tissues. The proportion of the esophageal tract that is exposed is set at 10%. Other tissues of interest were calculated at 100%.

Effective dose (*E*) is a calculation that permits comparison of the detriment of different exposures to ionizing radiation to an equivalent detriment produced by a full body dose of radiation. *E*, expressed in μSv, is calculated using the equation: $E = \Sigma\, w_T \times H_T$, where *E* is the summation of the products of the tissue weighting factor (w_T), which represents the relative contribution of that organ or tissue to the overall risk, and the radiation weighted dose H_T(7). The whole-body risk is determined by the summation of the radiation weighted doses to all tissues or organs exposed. ICRP 2007 weighting factors found in table 2 were used to calculate effective dose(7).

Tissue weighting factors used in the 2007 ICRP calculation of effective dose include 14 independently weighted tissues and a group of 14 remainder tissues(8). Because the uterus/cervix is present only in females, and prostate only in males, the number used in the weighted averaging of remainder tissues is 13.

In previous studies(3, 11), a RANDO phantom (radiation analog dosimetry system, Nuclear Associates, Hicksville, NY) and Thermoluminescent dosimeters (TLD) have been used for dosimetry. Because each RANDO is formed around an actual human skull, the attenuation characteristics for each RANDO varies from every other RANDO. An ATOM phantom was selected as a more reproducible model for comparative dosimetry. Effective doses were evaluated for standard and extended field cephalometric data runs and previously reported RANDO TLD data runs as well as unreported OSL runs. These were compared with the Adult ATOM phantom results of this study.

ANOVA of effective dose results was used to assess data for significant differences due to phantom type (Adult/Child), region of interest (dental/mandible/both arches/arches + TMJ/standard ceph), and scan protocol (QuickScan+/QuickScan/Standard/High Resolution). Where significant differences were found, Tukeys HSD test was used to determine which factors were significantly different from other factors. An alpha value of 0.05 was chosen for all tests.

Image quality indicators associated with FOV, scanning angle, kVp, and voxel size were acquired using a QUART DVT_AP phantom and QUART DVT_TEC software (QUART GmbH, Zorneding, Germany) (figure 5). The phantom consists of 16 cm diameter cylindrical slabs of Plexiglas with polyvinyl chloride and air elements configured to permit measurements of Poly-methyl-methacrylate (PMMA) voxel, PMMA Noise, Homogeneity, Contrast, Contrast to Noise Ratio (CNR), Modulation Transfer Function (MTF) 10%, MTF 50%, and Nyquist Frequency. Measurements are calculated in a user guided, semi-automatic manner from 2 DICOM slices selected from the volume. Each volume was measured 3 times and averages and standard deviations of each measurement parameter were calculated.

Results

Volumes produced by Atom and RANDO adult phantoms for 13 cm × 16 cm standard cephalometric and 17 cm × 23 cm extended fields of view are seen in figure 6. An unbiased estimator of difference between pairs ((A−B)/(A+B)/2) demonstrated that OSL dosimeter readings were 1.0% less than TLD readings for Standard Cephalometric fields and 2.5% less

NIH-PA Author Manuscript

NIH-PA Author Manuscript

for extended FOV RANDO imaging. The adult ATOM phantom effective doses were 0.2% less than RANDO doses for the Standard Cephalometric field and 0.8% less for the extended FOV.

ANOVA of combined adult and child phantom effective dose data demonstrated significant differences due to phantom ($p=0.0026$), region of interest ($p<.0001$), and exposure protocol ($p<.0001$). Considering QuickScan+, QuickScan, and Standard protocols, Child phantom doses were on average 36% greater than Adult phantom doses. Table 3 highlights effective dose results for the Adult phantom. The Tukey HSD test demonstrates that the QuickScan+ protocols resulted in significantly lower doses than Standard or High Resolution protocols, but was not statistically different from QuickScan protocols. The QuickScan protocol also resulted in lower doses than High Resolution protocols but was not statistically different from Standard protocols. 13×16 cm Cephalometric imaging resulted in statistically higher doses than all other fields of view. Similarly 6×16 cm maxillary imaging resulted in significantly lower doses than all other fields. Results for the 17×23 cm extended field of view (EFOV) are not included in table 3 because only standard and enhanced modes are available for this field. The effective dose for the Standard EFOV was 69 μSv while the Enhanced EFOV was 136 μSv.

Table 4 highlights effective dose results for the Child phantom. The Tukey HSD test demonstrates that the each scan protocol was significantly different from the other protocols with increasing dose occurring in order of QuickScan+, QuickScan, and Standard protocols. Maxillary FOVs produced statistically lower doses than arch + TMJ and 13 cmx16 cm cephalometric views. Figure 7 is a graphical representation of the data in table 3. Figure 8 is a graphical representation of the data in table 4.

Tables 5 and 6 provide equivalent doses to tissues and organs used in the calculation of effective dose. Absorbed doses in thyroid and brain are significantly greater in the child phantom than the adult phantom ($p<0.0001$).

Table 7 contains average parameter values and standard deviations from analysis of the QUART phantom images.

Increasing FOV diameter or increase in voxel size from .3 to .4 resulted in a 10% to 20% reduction in MTF. MTF 50% demonstrated a similar pattern of little response to mAs but provided 17% reduction in MTF with either increased FOV diameter from 8 cm to 16 cm or increase in voxel size from .3 to .4. As expected, smaller voxel sizes resulted in higher MTF values or better resolution.

Discussion

The majority of prior studies on CBCT dosimetry have used adult RANDO anthropomorphic phantoms (3, 12–14). However, it is understood that variations in mass, organ volume and organ position across the broad range of ages in the orthodontic patient population make it impossible to accurately estimate risk using a single type of dosimetry phantom (15). In this study we utilized both adult and 10 year old pediatric ATOM phantoms, allowing us to effectively bracket risk and thereby provide estimates that are applicable across the majority of the orthodontic patient population.

Another novel component of our study was the type of dosimeters that were used. Optically stimulated luminescent type dosimeters can be read within minutes of exposure, allow for multiple nondestructive reads, and can be erased and reused. This is significant considering this study would have required more than 1000 separate dosimeters had TLDs been used, some of which would have likely failed during the destructive read process. Hence, testing the many fields of view and exposure parameters possible in the i-CAT FLX would have been much less feasible without the use of OSL dosimeters. It was important to validate the results obtained with the ATOM phantoms and the OSL dosimeters by comparing them to the more common RANDO phantom and TLD data. The comparison of the different dosimeters and phantoms demonstrated differences of less than 2% in calculations of effective dose between TLD, and OSL based and in RANDO vs. ATOM phantoms. These results suggest that our current ATOM adult phantom results can be fairly compared with previous TLD results from a RANDO phantom.

There is no shortage of controversy surrounding CBCT in orthodontics. Some authors have expressed concern over the trend to use high dose, high resolution CBCT scans on young orthodontic patients as a substitute for stone study models or for the automated manufacture of custom appliances (16). Relevant to this issue, the results of our study demonstrate that effective doses were an average of 36% greater in the child phantom than in the adult. Not only is the effective dose one third higher, but due to the increased radiosensitivity of tissues, the risk is an additional 2–5× higher to a pediatric patient (5). This is important information to consider when making decisions about what type of diagnostic imaging might be best for patients. It is also important to consider the cause of differences in effective dose between the adult and child phantoms. An examination of the equivalent doses to each organ revealed that the increase in effective dose observed in the child is mostly due to the simulated anatomical position of the thyroid (Figure 9). The values calculated for thyroid dose are based on readings from two dosimeters positioned at level 10 of the Adult ATOM phantom. This is where the greatest bulk of the lobes and isthmus of the gland are located. This position is also analogous to the position of dosimeters used in the RANDO phantom, with the exception that both dosimeters are deep in the ATOM phantom while one dosimeter was superficial in the RANDO phantom. In contrast, thyroid dose calculation in the child phantom is based on two dosimeters in level 9 averaged with a single dosimeter in level 8. The rationale for this difference in dose measurement is based on the proximity of the thyroid gland to the lower border of the mandible, which is closer in children than adults (Figure 9). This proximity means that direct exposure of the thyroid is more likely in children than adults when the base of the FOV is situated just below the chin. Intensity of scatter radiation from jaw structures to the thyroid will also increase with the reduced distance of these structures in a child. Because the thyroid has a tissue weight of .04, this organ provides a significant contribution to the calculation of effective dose for head and neck exposures. With patients, direct thyroid exposure may be reduced by rotating the chin upward and positioning the lower border of the mandible parallel with the rotational plane of the beam (parallel to the floor); however, this strategy is not possible with the ridged phantoms utilized in this research. In addition to the chin-cup, this strategy also causes difficulties for those wishing to do cephalometric analysis of soft tissue profile, especially analysis of chin/neck/throat form.

After the consideration of patient positioning and proper field of view selection, our data demonstrates that optimization of exposure parameters and filtration can greatly reduce patient dose. Here we have shown that the QuickScan+ protocol provided a substantial 87% reduction in dose compared with Standard exposure protocols in both Child and Adult phantoms. Thus, when QuickScan+ protocols can be utilized, they will provide a clinically meaningful reduction in dose. The largest Quick Scan+ dose recorded in this study (18 μSv) was for the 13×16cm child cephalometric scan. This dose is little more than 2 days of US per capita background radiation. It is also two orders of magnitude less than a typical medical CT head scan. The full field of view QuickScan+ protocols are also less than the combined dose of representative modern digital 2-dimensional panoramic and cephalomatric radiographs (14–24 μS and 4 uS respectively) (13, 17). It is interesting to note that our testing of the 2D panoramic capabilities known as the iPAN demonstrated a dose of 24 uSv for both the adult and the child phantom (i-Cat Nextgen, unpublished).

Also noteworthy for discussion, the i-CAT FLX retains its Suresmile certification. In 2012 Grunheild et al conducted dosimetry of the Suresmile scan protocol using an i-CAT Nextgen (17). The Suresmile scan protocol requires the high resolution 0.2 mm voxel scan. Similar to Grunheild we found that a Suresmile scan of both arches (16×8 FOV) in an adult imparts an effective dose of 148μSv. We did not conduct high resolution imaging of the pediatric phantom, however we found that pediatric phantom doses were on average 36% greater than Adult phantom doses. Hence the estimated Suresmile dose for the average orthodontic patient likely falls between 148 μSv and 198 μSv.

In the quest to lower the dose of ionizing radiation administered to patients, dramatic reductions in dose are meaningless if image quality degrades to the point of being non-diagnostic. As optimization and dose reduction become more of a focus for CBCT manufactures, the effects on image quality will need close attention. Published evidence establishing the usability of low dose/low quality scans for diagnostic purposes in dentistry or in orthodontics is limited. However one potential application specific to orthodontics would be a midtreatment scan to evaluate root angulations. Additional studies are needed to confirm that other important information present in 2D imaging or higher dose scans such as gross advances in periodontal conditions, changes in root length and changes in morphology that indicate patterns of resorption are not lost in these low dose scans.

Germany is the first country to develop national standards for image quality testing of dental CBCT devices (DIN 6868-161:2013-01). The QUART DVT phantom is the first commercially available phantom which complies with those standards. In this study we evaluated the effect of the new Quickscan+ protocols on the objective components of image quality CNR and MTF using the QUART DVT phantom. Our data demonstrated that when voxel size and FOV are held constant, an increase in CNR is seen with increasing energy and mAs (QuickScan+ < QuickScan < Standard). Changes in CNR have been shown to generally correlate with observer impressions of an image (18). As CNR increases the general impression of how an image appears improves. Changes in Voxel size and FOV also influences CNR. As expected, our data demonstrated that increasing the diameter of the FOV resulted in a modest reduction in CNR, while increasing the size of the voxel from .3 to .4 mm resulted in an increase in CNR. Interestingly, with High Resolution scans increasing voxel size from .125 to .25 revealed a slight trend of increased CNR. This is not dramatic and may not be clinically significant. It is important to note that is that the reduction of energy and mAs from the QuickScan to the QuickScan+ protocols reduced the effective dose to patients by a factor of 4, but only reduced CNR by a factor of 2. Hence the reduction of energy and mAs in the i-CAT FLX was an effective way to reduce patient dose in exchange for a modest reduction in the image quality as measured by CNR. In comparison, the objective measure of resolution, MTF was not as sensitive to the effects of mAs but was more sensitive to increases in FOV diameter and voxel size. Although CNR and MTF can be correlated to subjective image quality(6), additional research to evaluate the influence of CNR and MTF on diagnostic efficacy is needed.

Conclusions

The results of this study reflect a large range of imaging options that can be tailored to specific regions of interest. A variety of exposure options are also available to adjust exposure levels to accommodate a range of diagnostic tasks. Use of QuickScan and QuickScan+ imaging protocols and smaller fields of view result in significant patient dose reductions over alternate larger fields or Standard or High Resolution protocols.

Practitioners may be guided by selection criteria in deciding which orthodontic patients are most likely to benefit from a radiographic examination and which examination is most likely to provide needed information. Such guidelines consider the balance of benefit and potential harm from diagnostic imaging. A working group of orthodontists and oral and maxillofacial radiologists has developed initial guidelines that have been adopted in a position paper by the American Academy of Oral and Maxillofacial Radiology.[19] Determination of which exposure protocol is appropriate for a specific diagnostic task awaits further research. Contrast to noise ratio data in conjunction with modulation transfer function indications of resolution limits may serve as a useful guide in indicating the utility of different scanning parameters for specific diagnostic tasks.

Acknowledgments

This research was supported in part by the National Institute of Dental and Craniofacial Research of the National Institutes of Health under award number R21DE022160. The content is solely the responsibility of the authors and does not necessarily represent the official views of the National Institutes of Health.

Travel support and an honorarium were provided to Dr. Ludlow by Imaging Sciences.

References

1. Kapila S, Conley RS, Harrell WE Jr. The current status of cone beam computed tomography in orthodontics. Dentomaxillofac Radiol. 2011 Jan.40:24–34. [PubMed: 21159912]
2. Smith-Bindman R, Lipson J, Marcus R, Kim KP, Mahesh M, Gould R, et al. Radiation dose associated with common computed tomography examinations and the associated lifetime attributable risk of cancer. Arch Intern Med. 2009 Dec 14.169:2078–86. [PubMed: 20008690]
3. Ludlow JB, Ivanovic M. Comparative dosimetry of dental CBCT devices and 64-slice CT for oral and maxillofacial radiology. Oral Surg Oral Med Oral Pathol Oral Radiol Endod. 2008 Jul.106:106–14. [PubMed: 18504152]
4. Brenner DJ, Hall EJ. Computed tomography--an increasing source of radiation exposure. N Engl J Med. 2007 Nov 29.357:2277–84. [PubMed: 18046031]
5. Brenner D, Elliston C, Hall E, Berdon W. Estimated risks of radiation-induced fatal cancer from pediatric CT. AJR Am J Roentgenol. 2001 Feb.176:289–96. [PubMed: 11159059]
6. Watanabe H, Honda E, Tetsumura A, Kurabayashi T. A comparative study for spatial resolution and subjective image characteristics of a multi-slice CT and a cone-beam CT for dental use. Eur J Radiol. 2011 Mar.77:397–402. [PubMed: 19819091]
7. Valentin J. The 2007 Recommendations of the International Commission on Radiological Protection. Publication 93. Ann ICRP. 2007; 37:1–332.
8. Underhill TE, Chilvarquer I, Kimura K, Langlais RP, McDavid WD, Preece JW, et al. Radiobiologic risk estimation from dental radiology. Part I. Absorbed doses to critical organs. Oral Surg Oral Med Oral Pathol. 1988 Jul.66:111–20. [PubMed: 3165508]
9. Cristy M. Active bone marrow distribution as a function of age in humans. Phys Med Biol. 1981 May.26:389–400. [PubMed: 7243876]
10. NBS handbook no. 85. Anonymous US Government Printing Office; 1963. Physical aspects of irradiation.
11. Ludlow JB, Davies-Ludlow LE, Brooks SL. Dosimetry of two extraoral direct digital imaging devices: NewTom cone beam CT and Orthophos Plus DS panoramic unit. Dentomaxillofac Radiol. 2003 Jul.32:229–34. [PubMed: 13679353]
12. Ludlow JB, Davies-Ludlow LE, Brooks SL, Howerton WB. Dosimetry of 3 CBCT devices for oral and maxillofacial radiology: CB Mercuray, NewTom 3G and i-CAT. Dentomaxillofac Radiol. 2006 Jul.35:219–26. [PubMed: 16798915]
13. Ludlow JB, Davies-Ludlow LE, White SC. Patient risk related to common dental radiographic examinations: the impact of 2007 International Commission on Radiological Protection recommendations regarding dose calculation. J Am Dent Assoc. 2008 Sep.139:1237–43. [PubMed: 18762634]

14. Pauwels R, Beinsberger J, Stamatakis H, Tsiklakis K, Walker A, Bosmans H, et al. Comparison of spatial and contrast resolution for cone-beam computed tomography scanners. Oral Surg Oral Med Oral Pathol Oral Radiol. 2012 Jul.114:127–35. [PubMed: 22727102]
15. Cassola VF, Milian FM, Kramer R, de Oliveira Lira CA, Khoury HJ. Standing adult human phantoms based on 10th, 50th and 90th mass and height percentiles of male and female Caucasian populations. Phys Med Biol. 2011 Jul 7.56:3749–72. [PubMed: 21628776]
16. Bogdanich, WMJ. The New York Times. 2010 Nov 23. Radiation worries for children in dentists' chairs. (NY ed)Sect. A:1
17. Grunheid T, Kolbeck Schieck JR, Pliska BT, Ahmad M, Larson BE. Dosimetry of a cone-beam computed tomography machine compared with a digital x-ray machine in orthodontic imaging. Am J Orthod Dentofacial Orthop. 2012 Apr.141:436–43. [PubMed: 22464525]
18. Lin, Y.; Wang, X.; Sehnert, WJ.; Foos, DH.; Barski, L.; Samei, E. Quantification of radiographic image quality based on patient anatomical contrast-to-noise ratio: a preliminary study with chest images. Medical Imaging 2010: Image Perception, Observer Performance, and Technology Assessment; Proc. SPIE; March 03, 2010; p. 76271F
19. American Academy of Oral and Maxillofacial Radiology. Clinical Recommendations Regarding Use of Cone Beam Computed Tomography (CBCT) in Orthodontics. Position Statement by the American Academy of Oral and Maxillofacial Radiology. Oral Surg Oral Med Oral Pathol Oral Radiol. 2013 Aug.116:238–257. [PubMed: 23849378]

OSL ID No.	Adult Phantom Location (level of OSLD location)
1	Calvarium anterior (2)
2	Mid brain (2)
3	Calvarium left (3)
4	Mid brain (3)
5	Calvarium posterior (4)
6	Pituitary (4)
7	Right lens of eye (4-5)
8	Left lens of eye (4-5)
9	Right ethmoid (5
10	Left maxillary sinus (6)
11	Oropharyngeal airway (7)
12	Right parotid (7)
13	Left parotid (7)
14	Right ramus (7)
15	Left ramus (7)
16	Left back of neck (8)
17	Right submandibular gland (8)
18	Left submandibular gland (8)
19	Center sublingual gland (8)
20	Center C spine (8)
21	Lateral neck - left (9)
22	Thyroid – left (10)
23	Thyroid - right (10)
24	Esophagus (10)

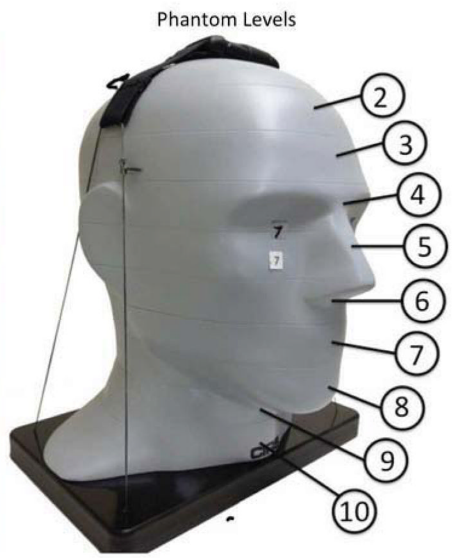

Figure 1.
Locations of optically stimulated luminescent dosimeters (OSLD) in adult Atom Max Model 711 phantom

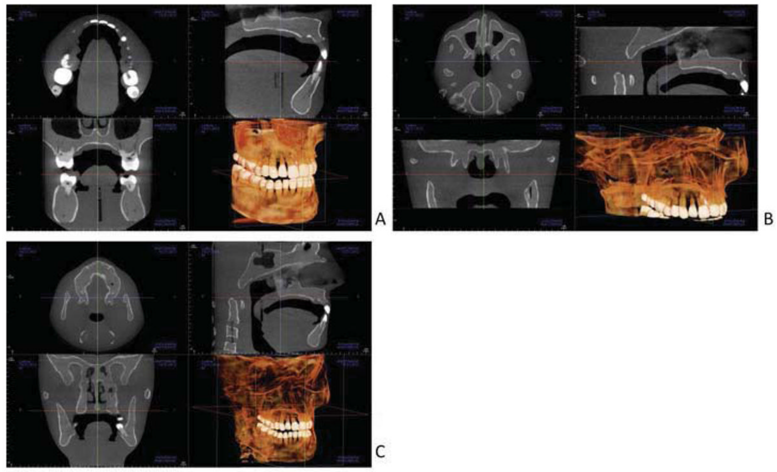

Figure 2.
Adult phantom demonstrating positioning principles for phantom scanning: A) lower border of volume is 5 mm below bony chin; anterior border of volume is 5 mm anterior to central incisors. This positioning was used on dental (8×8 cm High resolution scan seen here), mandible, both arches, and arches + TMJ scans. B) lower border of volume is 5 mm below central incisal edge; anterior border of volume is 5 mm anterior to central incisors. This positioning was used on maxilla volumes (6×16 cm High resolution scan seen here). C) tip of the nose and lower soft tissue border of the chin are included in the field of view for standard cephalometric volumes (13×16 cm High resolution scan seen here) and extended field of view (EFOV) volumes.

NIH-PA Author Manuscript

NIH-PA Author Manuscript

OSL ID No.	Child Phantom Location (level of OSLD location)
1	Calvarium anterior (2)
2	Calvarium left (2)
3	Calvarium posterior (2)
4	Mid brain (2)
5	Mid brain (3)
6	Pituitary (4)
7	Right orbit (4)
8	Right lens of eye (4-5)
9	Left lens of eye (4-5)
10	Right maxillary sinus (5)
11	Left nasal airway (5)
12	Right parotid (6)
13	Left parotid (6)
14	Left back of neck (6)
15	Right ramus (7)
16	Left ramus (7)
17	Right submandibular gland (7)
18	Left submandibular gland (7)
19	Center sublingual gland (7)
20	Center C spine (8)
21	Thyroid superior–left (8)
22	Thyroid – left (9)
23	Thyroid - right (9)
24	Esophagus (9)

Figure 3.
CIRS 10 year-old child phantom dosimeter locations

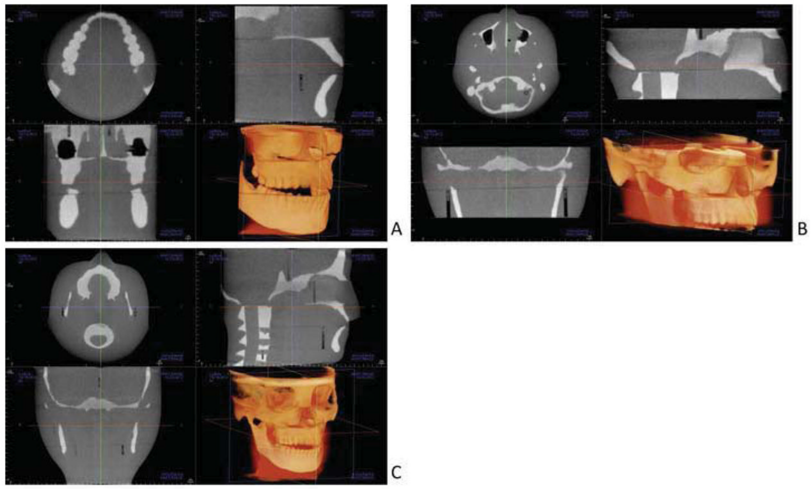

Figure 4.
Child phantom demonstrating positioning principles for phantom scanning: A) lower border of volume is 5 mm below bony chin; anterior border of volume is 5 mm anterior to central incisors. This positioning was used on dental (8×8 cm High resolution scan seen here), mandible, and both arches. B) lower border of volume is 5 mm below central incisal edge; anterior border of volume is 5 mm anterior to central incisors. This positioning was used on maxilla volumes (6×16 cm High resolution scan seen here). C) tip of the nose and lower soft tissue border of the chin are included in the field of view for standard cephalometric volumes (13×16 cm High resolution scan seen here) and arches + TMJ scans.

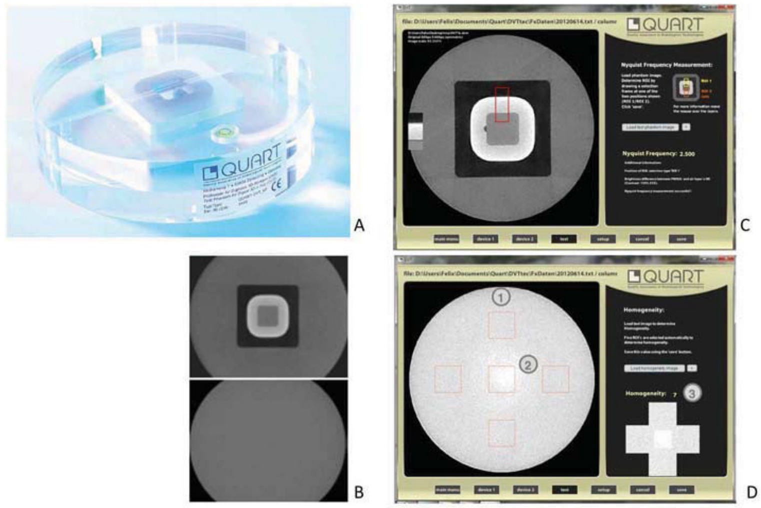

Figure 5.
Quart DVT_AP CBCT image quality system: A) phantom, B) Sample axial images of aluminum and air elements (top) and plexiglass layer (bottom), C) analysis software window for calculation of Nyquist frequency, D) analysis software window for calculating Homogeneity

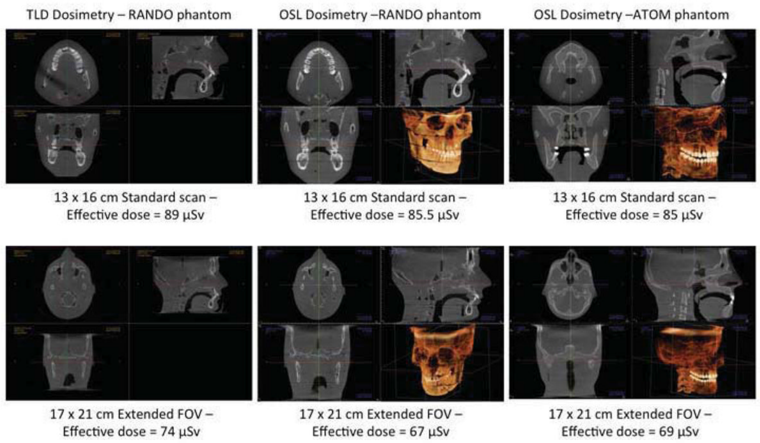

Figure 6.

Comparison of adult RANDO and ATOM phantoms, TLD and OSL dosimeter, Standard cephalometric and Extended FOVs

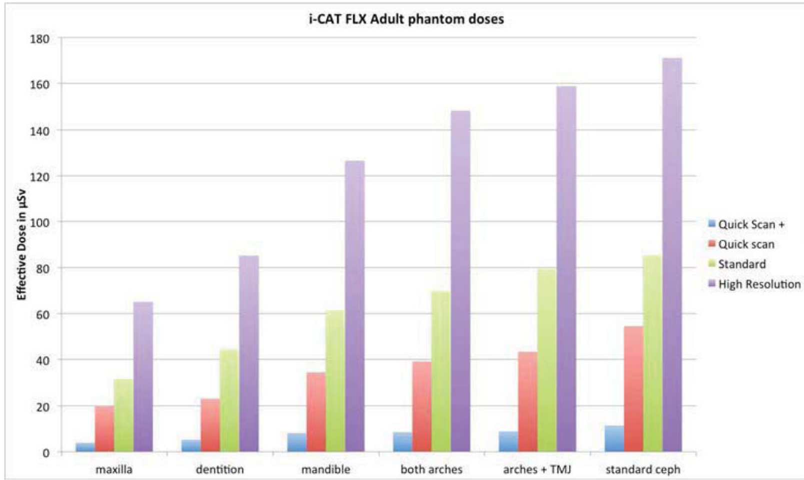

Figure 7.
Adult phantom effective dose by scan type and FOV

NIH-PA Author Manuscript
NIH-PA Author Manuscript

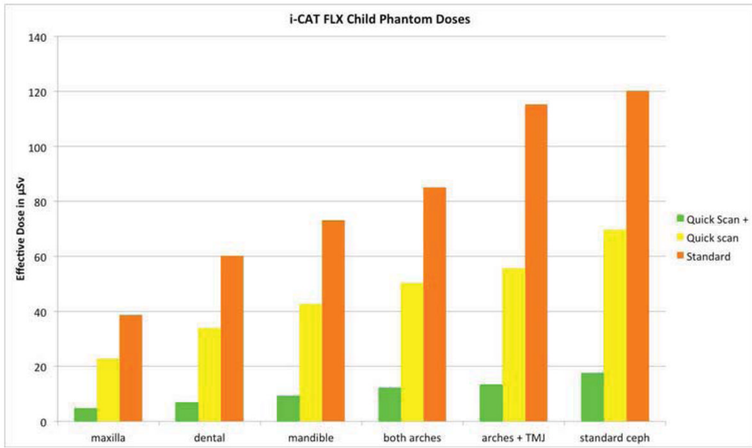

Figure 8.
Alternate depiction of Child phantom effective dose by exposure protocol and FOV

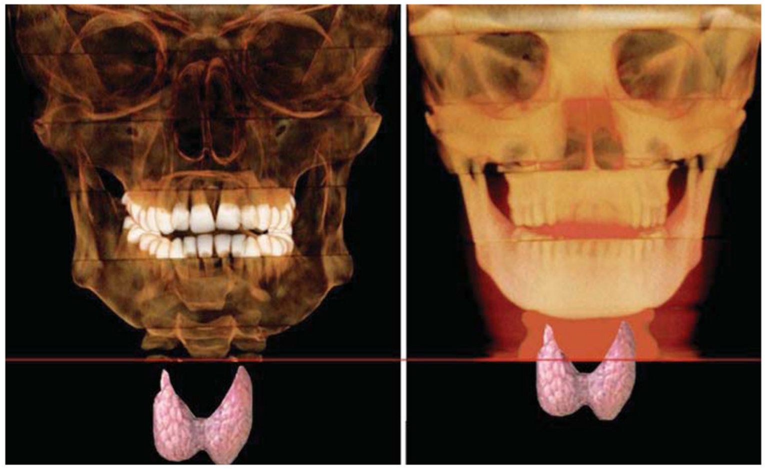

Figure 9.
Comparison of thyroid level in child and adult. Red line denotes lower edge of volume.

Table 1

Dosimetry plan for recording of Adult and Child phantom effective dose for iCAT NG programs and exposure settings.

FOV	ROI	Protocol	Scan angle	Basis Image Frames	Voxel size	Adult Phantom	Child Phantom	kVp	mA	Exposure (seconds)
8×8	dental	Quick scan +	180	160	0.3/0.4	A	C	90	3	2
16×6	maxilla	Quick scan +	180	160	0.3/0.4	A	C	90	3	2
16×6	mandible	Quick scan +	180	160	0.3/0.4	A	C	90	3	2
16×8	both arches	Quick scan +	180	160	0.3/0.4	A	C	90	3	2
16×11	arches + TMJ	Quick scan +	180	160	0.3/0.4	A	C	90	3	2
16×13	standard ceph	Quick scan +	180	160	0.3/0.4	A	C	90	3	2
16×6	maxilla	Quick scan	180	160	0.3/0.4	A	C	120	5	2
8×8	dental	Quick scan	180	160	0.3/0.4	A	C	120	5	2
16×13	standard ceph	Quick scan	180	160	0.3/0.4	A	C	120	5	2
16×8	both arches	Quick scan	180	160	0.3/0.4	A	C	120	5	2
16×11	arches + TMJ	Quick scan	180	160	0.3/0.4	A	C	120	5	2
16×6	mandible	Quick scan	180	160	0.3/0.4	A	C	120	5	2

FOV	ROI	Protocol	Scan angle	Basis Image Frames	Voxel size	Adult Phantom	Child Phantom	kVp	mA	Exposure (seconds)
8×8	dental	Standard	360	300	0.3/0.4	A	C	120	5	3.7
16×6	maxilla	Standard	360	300	0.3/0.4	A	C	120	5	3.7
16×6	mandible	Standard	360	300	0.3/0.4	A	C	120	5	3.7
16×8	both arches	Standard	360	300	0.3/0.4	A	C	120	5	3.7
16×11	arches + TMJ	Standard	360	300	0.3/0.4	A	C	120	5	3.7
16×13	standard ceph	Standard	360	300	0.3/0.4	A	C	120	5	3.7
8×8	dental	High resolution	360	600	0.125/0.20/0.25	A		120	5	7.4
16×6	maxilla	High resolution	360	600	0.125/0.20/0.25	A		120	5	7.4
16×6	mandible	High resolution	360	600	0.125/0.20/0.25	A		120	5	7.4
16×8	both arches	High resolution	360	600	0.125/0.20/0.25	A		120	5	7.4
16×11	arches + TMJ	High resolution	360	600	0.125/0.20/0.25	A		120	5	7.4
16×13	standard ceph	High resolution	360	600	0.125/0.20/0.25	A		120	5	7.4
23×17	EFOV	Standard	360	300	0.3/0.4	A		120	5	3.7
23×17	EFOV	Enhanced	360	600	0.3/0.4	A		120	5	7.4

Gray highlight = actual voxel size used in this study

Table 2

Estimated percentage of tissue irradiated, ICRP weighting factor for calculation of Effective dose, and TLDs used to calculate mean absorbed dose to a tissue or organ of an Adult or 10 year-old Child phantom

	Fraction irradiated Adult	OSL ID (see Figure 1)	ICRP 2007 w_T	Fraction Irradiated Child	OSL ID (see Figure 3)
Bone Marrow	12.2%		0.12	15.4%%	
mandible	0.8%	14, 15		1.1%%	15, 16
calvaria	7.7%	1, 3, 5		11.6%	1, 2, 3
cervical spine	3.8%	20		2.7%	20
thyroid	100%	22, 23	0.04	100%	21, 22, 23
esophagus	10%	24	0.04	10%	24
skin	5%	7, 8, 16	0.01	5%	8, 9, 14
Bone surface*	16.5%		0.01	16.5%	
mandible	1.3%	14, 15		1.3%	15, 16
calvaria	11.8%	1, 3, 5		11.8%	1, 2, 3
cervical spine	3.4%	20		3.4%	20
Salivary glands	100%		0.01	100%	
parotid	100%	12, 13		100%	12, 13
submandibular	100%	17, 18		100%	17, 18
sub-lingual	100%	19		100%	19
Brain	100%	2, 4, 6	0.01	100%	4, 5, 6
Remainder			0.12		
lymphatic nodes	5%	11–13, 17–19, 21–24		5%	12–13, 17–19, 21–24
muscle	5%	11–13, 17–19, 21–24		5%	12–13, 17–19, 21–24
extrathoracic region	100%	9–13, 17–19, 21–24		100%	10–13, 17–19, 21, 24
oral mucosa	100%	11–13, 17–19		100%	12–13, 17–19

* Bone surface dose = bone marrow dose × bone/muscle mass energy absorption coefficient ratio = −0.0618 × 2/3 kV peak + 6.9406 using data taken from NBS Handbook No. 85.[10]

NIH-PA Author Manuscript
NIH-PA Author Manuscript

Table 3

Effective doses for Adult phantom by exposure protocol and field of view - ANOVA p value and Tukey HSD maxilla dentition mandible

	maxila	dentition	mandible	both arches	arches + TMJ	standard ceph	average	ANOVA p=.0055 Tukey HSD*
Quick Scan +	4	5	8	8	9	11	8	C
Quick Scan	20	23	34	39	43	54	36	BC
Standard	32	44	61	70	79	85	62	B
High Resolution	65	85	127	148	159	171	126	A
average	30	39	58	66	73	81	58	
ANOVA p<.0001 - Tukey HSD*	C	BC	ABC	ABC	AB	A		

* Levels not connected by same letter are significantly different

Table 4

Effective doses for Child phantom by exposure protocol and field of view. The ANOVA p value and Tukey HSD maxilla dental mandible

	maxila	dental	mandible	both arches	arches + TMJ	standard ceph	average	ANOVA p=.0167 Tukey HSD*
Quick Scan +	5	7	9	12	13	18	11	A
Quick Scan	23	34	43	50	56	70	46	B
Standard	39	60	73	85	115	120	82	C
average	22	34	42	49	61	69	46	
ANOVA p<.0001 -Tukey HSD*	B	AB	AB	AB	A	A		

*Levels not connected by same letter are significantly different

NIH-PA Author Manuscript
NIH-PA Author Manuscript

Table 5

Equivalent Dose measurements on an adult phantom for i-CAT FLX by field of view, region of interest, and scanning protocol

				Weighted Components of Effective Dose Calculation Group Components								Remainder Group Components			
FOV (cm)	**Region of Interest**	**Protocol**	**Effective dose**	**Bone Marrow**	**Thyroid**	**Esophagus**	**Skin**	**Bone surface**	**Salivary glands**	**Brain**	**Remainder average**	**Lymphatic nodes**	**Extrathoracic airway**	**Muscle**	**Oral mucosa**
8×8	dentition	Quick Scan +	5.3	4	22	2	2	15	142	4	18	5	90	5	133
16×6	maxilla	Quick Scan +	3.9	4	9	1	1	15	96	13	15	4	73	3	112
16×6	mandible	Quick Scan +	8.1	9	36	5	4	30	193	6	25	7	121	7	195
16×8	both arches	Quick Scan +	8.5	9	38	5	4	32	196	9	27	7	132	7	200
16×11	arches + TMJ	Quick Scan +	8.8	9	36	4	5	33	207	19	29	8	146	7	214
16×13	standard ceph	Quick Scan +	11.4	12	48	6	8	43	252	44	36	10	186	9	261
8×8	dentition	Quick scan	23	19	112	10	8	42	596	28	76	20	384	20	561
16×6	maxilla	Quick scan	19.7	19	68	8	5	46	463	65	72	18	356	16	542
16×6	mandible	Quick scan	34.5	39	164	19	17	81	808	30	109	31	528	30	824
16×8	both arches	Quick scan	39.2	44	177	22	19	92	917	57	125	34	621	34	942
16×11	arches + TMJ	Quick scan	43.4	50	193	24	26	107	972	123	137	37	701	36	1004
16×13	standard ceph	Quick scan	54.5	56	257	30	39	123	1194	216	171	47	907	46	1220
8×8	dentition	Standard	44.5	31	222	22	12	71	1172	58	149	40	780	38	1079
16×6	maxilla	Standard	31.6	29	101	12	11	73	719	131	119	29	629	25	867
16×6	mandible	Standard	61.3	59	290	33	18	124	1567	51	198	54	944	53	1519
16×8	both arches	Standard	69.8	70	329	40	23	150	1693	95	225	61	1131	60	1677
16×11	arches + TMJ	Standard	79.4	81	353	43	41	176	1859	238	256	67	1333	65	1861
16×13	standard ceph	Standard	85.3	83	405	48	74	185	1898	380	265	71	1433	69	1875
8×8	dentition	High resolution	85.1	62	434	42	23	139	2237	115	279	75	1470	73	2012
16×6	maxilla	High resolution	65	60	204	23	28	152	1488	276	244	59	1258	52	1809
16×6	mandible	High resolution	126.5	126	620	72	40	263	3131	101	403	114	1972	113	3043
16×8	both arches	High resolution	148.1	148	735	81	50	315	3527	199	473	131	2375	128	3518
16×11	arches + TMJ	High resolution	158.8	161	747	86	71	350	3641	452	508	136	2677	131	3667
16×13	standard ceph	High resolution	171.1	163	821	96	145	365	3809	728	537	144	2899	140	3794
23×17	Extended FOV	Standard	69.2	84	301	39	50	202	1293	668	195	53	1038	49	1391
23×17	Extended FOV	Enhanced	136.2	170	608	74	97	408	2530	1282	378	103	2027	97	2690

NIH-PA Author Manuscript
NIH-PA Author Manuscript

Table 6

Equivalent Dose measurements on a 10-year-old child phantom for i-CAT FLX by field of view, region of interest, and scanning protocol

				Weighted Components of Effective Dose Calculation Group								Remainder Group Components			
FOV (cm)	Region of Interest	Protocol	Effective dose	Bone Marrow	Thyroid	Esophagus	Skin	Bone surface	Salivary glands	Brain	Remainder average	Lymphatic nodes	Extrathoracic airway	Muscle	Oral mucosa
16×6	maxilla	Quick Scan +	4.7	2	20	1	7	7	115	25	18	4	93	4	128
8×8	dental	Quick Scan +	6.8	3	45	2	3	13	163	12	22	5	116	5	163
16×6	mandible	Quick Scan +	9.4	5	78	4	5	21	189	9	27	7	137	7	197
16×8	both arches	Quick Scan +	12.3	8	117	5	5	32	212	15	31	8	167	8	222
16×11	arches + TMJ	Quick Scan +	13.3	9	121	5	9	34	221	52	34	9	186	9	233
16×13	standard ceph	Quick Scan +	17.5	12	160	8	11	46	277	98	42	11	235	11	292
16×6	maxilla	Quick scan	22.8	11	102	7	31	24	541	130	82	19	440	19	592
8×8	dental	Quick scan	33.9	18	242	12	13	42	762	69	106	26	557	26	769
16×6	mandible	Quick scan	42.6	26	355	18	23	64	856	50	122	32	625	32	895
16×8	both arches	Quick scan	50.3	31	412	20	26	74	973	142	143	36	758	36	1023
16×11	arches + TMJ	Quick scan	55.6	36	417	22	42	84	1045	330	156	39	845	39	1103
16×13	standard ceph	Quick scan	69.6	51	637	30	43	120	1085	429	166	44	935	44	1138
16×6	maxilla	Standard	38.7	19	158	11	69	43	889	252	142	30	820	30	969
8×8	dental	Standard	60.1	33	403	20	20	77	1401	134	191	45	1059	45	1331
16×6	mandible	Standard	73.2	41	530	30	34	98	1654	106	224	57	1133	57	1670
16×8	both arches	Standard	85.1	53	659	35	39	126	1754	192	248	62	1343	62	1763
16×11	arches + TMJ	Standard	115.1	80	1001	53	81	190	2045	391	302	77	1713	77	2060
16×13	standard ceph	Standard	120.1	91	1003	53	82	211	2038	731	303	77	1729	77	2054

Table 7

QUART phantom image measurements

Protocol	QuickScan +	Quick Scan	Standard	High resolution	High resolution	High resolution	QuickScan +	QuickScan	Standard	Quick Scan +	QuickScan	Standard	High resolution half scan	High resolution half scan
FOV	8×8	8×8	8×8	8×8	8×8	8×8	16×8	16×8	16×8	16×8	16×8	16×8	8×8	8×8
Scan angle	180	180	360	360	360	360	180	180	360	180	180	360	180	180
Voxel size	0.3	0.3	0.3	0.125	0.2	0.25	0.3	0.3	0.3	0.4	0.4	0.4	0.2	0.25
	Average of 3 measurements													
PMMA voxel	709.4	742.1	733	734.5	741.7	740.4	864.7	889.6	890.4	861.1	890.5	886.9	743.7	725.4
PMMA Noise	105.1	52.5	38.2	88.7	90.7	88.5	96.6	50.8	37.7	95.6	50.4	37.1	122.8	122.4
Homogeneity	17	18	49	52	63	60	15.7	16	16	17.7	17	15.7	15.3	17
Contrast	722.7	724.2	690.4	632.1	644.6	714.6	629	649	627.3	715.5	673.7	635.5	637	723.6
CNR	7.7	16.3	22.3	7	7.6	9	5.8	11.4	20.6	8.2	16.7	18.2	4.8	6.4
MTF 10%	1	1.1	1.1	1.6	1.3	1.3	0.9	0.9	0.9	0.9	0.9	0.9	1.7	1.6
MTF 50%	0.6	0.6	0.6	0.9	0.8	0.7	0.5	0.5	0.5	0.5	0.5	0.5	1	0.9
Nyquist Frequency	1.7	1.7	1.7	4	2.5	2	1.6	1.6	1.7	1.3	1.3	1.2	2.5	2
	Standard deviation of measurements													
PMMA voxel	1.8	4.8	2.9	1	5.1	0.2	2.5	0.9	0.6	1.2	0.3	0.5	33.5	0.6
PMMA Noise	0.7	0.6	0.3	0.8	1.4	1	2.2	0.1	2.1	0.9	0.7	1.3	0.5	1
Homogeneity	1	1	4.4	6.1	16.1	2.6	1.2	1	1	1.2	1	0.6	0.6	1
Contrast	28.9	62.5	6.5	16.9	32.7	56.4	43.8	35.8	40.8	43.9	50.9	35.2	4.5	37.4
CNR	1.1	3.1	2.2	0.8	0.5	1.4	0.3	0.6	1.3	0.5	4.1	0.1	0.4	0.8
MTF 10%	0	0.2	0.1	0.1	0.2	0.4	0	0	0	0.1	0	0	0	0
MTF 50%	0	0	0	0.1	0.1	0.2	0	0	0	0.1	0	0	0	0
Nyquist Frequency	0	0	0	0	0	0	0	0	0	0	0	0	0	0